Electronic Supplementary Material (ESI) for ChemComm.

Supporting Information: Thermal properties of single-layer MoS_2-WS_2 alloys enabled by machine-learned interatomic potentials

Juan M. Marmolejo-Tejada and Martín A. Mosquera*

Department of Chemistry and Biochemistry, Montana State University, Bozeman, MT 59717 USA.

E-mail: martinmosquera@montana.edu

Moment Tensor Potential (MTP) model and training

As detailed in ref.[1] the MTP energy expression is given by eq. 1:

$$E^{MTP}(\boldsymbol{b}_j) = \sum_{i \in \text{ Neighborhoods}} V(\boldsymbol{n}_i) \tag{1}$$

where V is the interatomic potential in a given interaction neighborhood and is seen as a family of functions with different number of arguments. It is required to follow permutation, rotation and reflection invariance, needs to be smooth with respect to atoms in the interaction neighborhood, and is defined as:

$$V(\boldsymbol{n}_i) = \sum_{\alpha \in \text{ basis}} \xi_\alpha B_\alpha(\boldsymbol{n}_i) \tag{2}$$

In eq. 2, $\{\xi_\alpha\}$ are the trainable coefficients, obtained with a regularized linear regression based on the energy, all the forces, and stress tensor. $\{B_\alpha\}$ are the basis functions, which are obtained as contracted products of the moments tensors:

$$B_\alpha = \prod_{\mu,\nu \,\in\, \text{levels}} M_{\mu,\nu} \tag{3}$$

where $\{M_{\mu,\nu}\}$ are such moment tensors, obtained with f_μ control functions, based on Chebyshev polynomials, and are defined as:

$$M_{\mu,\nu} = \sum_j f_\mu(r_{ij}, Z_i, Z_j) \underbrace{\boldsymbol{r}_{ij} \otimes ... \otimes \boldsymbol{r}_{ij}}_{\nu \text{ times}} \tag{4}$$

where $\boldsymbol{r}_{ij} \otimes ... \otimes \boldsymbol{r}_{ij}$ is the Kronecker product of ν copies of the vector $\boldsymbol{r}_{ij} \in \mathbb{R}^d$, assuming $\mathbb{R}^d$ is a smooth function.

As discussed in the main text, our training set consisted of 780 1L configurations that included pristine and alloyed systems, as follows:

- MoS_2 unit cell (see Figure S1 (a)): 300 configurations consisting of 1×1×1, 2×2×1, 3×3×1, 4×4×1 and 5×5×1 supercell repetitions, 60 each.
- WS_2 unit cell (see Figure S1 (b)): 300 configurations consisting of 1×1×1, 2×2×1, 3×3×1, 4×4×1 and 5×5×1 supercell repetitions, 60 each.
- $Mo_{0.5}W_{0.5}S_2$ unit cell (see Figure S1 (c)): 120 configurations consisting of 1×1×1 and 2×2×1 supercell repetitions, 60 each.
- $Mo_{0.5}W_{0.5}S_2$ 5×5×1 supercell (see Figure S1 (d)): 60 configurations.

The unit cells that are shown in Figure S1 are hexagonal with lattice vectors $a_1 = a_2 = 3.1604$ Å for MoS_2, $a_1 = a_2 = 3.1532$ Å for WS_2, based on the experimental values. For the alloys, we constructed $Mo_{0.5}W_{0.5}S_2$ configurations with random distribution of Mo and W atoms, and lattice vectors $a_1 = a_2 = 6.3136$ Å for the 2×2×1 system in Figure S1(c) and

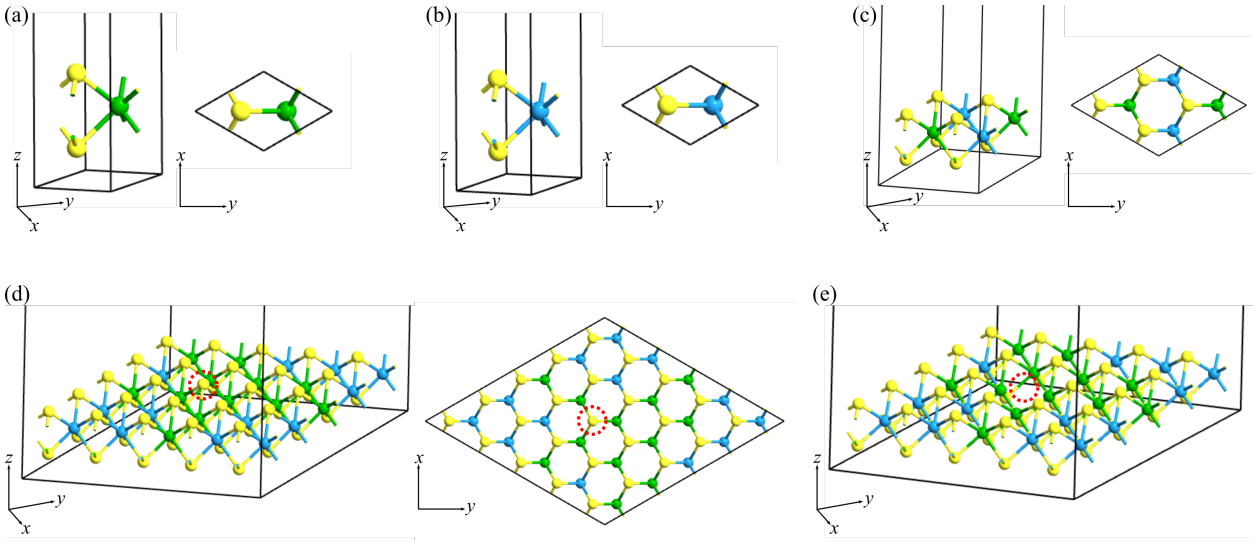

Figure S1: Unit cells used for 1L- (a) MoS_2, (b) WS_2 and (c) $Mo_{0.5}W_{0.5}S_2$ training configurations. (d) 5×5×1 $Mo_{0.5}W_{0.5}S_2$ supercell used in the training set. (e) Alloy configuration in (d) with a single sulfur vacancy, indicated by the red-dashed circle. Blue, green and yellow spheres correspond to W, Mo and S atoms, respectively.

$a_1 = a_2 = 15.784$ Å for the 5×5×1 system in Figure S1(d). We added 30 Å of vacuum to all the configurations for avoiding interactions with their periodic replicas in a_3.

40 out of the 60-configuration sets were obtained by adding small random displacements to the atomic coordinates in the supercell with up to 0.15 Å atomic rattling amplitude and expanding/contracting the lattice vectors within ±5%. The remaining 20 configurations of each set were obtained with MD trajectories of the supercell, with lattice vectors contracted/expanded by ±10%, under the canonical ensemble (NVT), using a Langevin thermostat and a friction constant of 0.01 fs^{-1}. Temperature was increased from 1 to 1000K during 100 fs, with a 1 fs time step, and 1 sample was extracted every 10 frames. Overall, 20% of the structures are used for testing.

We obtained the corresponding energies, forces and stresses for each configuration with DFT, using the LCAO (linear combination of atomic orbitals), as implemented in the QuantumATK package,[2,3] where the Kohn-Sham (KS) Hamiltonian is represented in the basis of double-zeta polarized (DZP) orbitals on all atoms, using a density mesh cut-off of 125 Hartree and a 4 Å k-point density along a_1 and a_2. The electron-core interactions are

described with the Perdew-Burke-Ernzerhof (PBE) parametrization of the generalized gradient approximation (GGA).[4] We minimized the atomic coordinates with a 10^{-3} eV and 10^{-2} eV/Å energy and force criteria, respectively.

The fitted MTP contained 2000 basis functions with an outer cutoff radius of 6 Å for each element pair. The root-mean-square deviation (RMSE) obtained in the optimization of the non-linear coefficients is summarized in Table S2 for both, training and testing.

Table S1: RMSE for energies, forces and stresses, obtained for the training (80%) and testing (20%) configurations.

	Training	Testing
Energy/atom (eV)	0.0012	0.0017
Force (eV/Å)	0.0310	0.0312
Stress (eV/Å^3)	0.0017	0.0019

Phonon dispersion of fully relaxed structures

As discussed in the main text, the trained MTP potential shows very good agreement with the DFT calculations. This includes capturing a "negative" energy band near the acoustic mode. This is merely an artifact of the training, but it attests to its validity. As we show in Figure S2, the MTP acoustic modes are positive, when the atomic positions and lattice parameters are fully optimized (see Table). Nonetheless, the chosen DFT functional and self-consistent convergence criteria result in a reduction of $\sim 20 - 30\ cm^{-1}$ in the frequency of the optical modes.

Additionally, to test the stability of the trained MTP for alloy configurations with sulfur vacancies, we remove a single S atom to the $Mo_{0.5}W_{0.5}S_2$ configuration in Figure S1(d), as marked by the red-dashed circle, and perform full optimization of lattice parameters and coordinates, resulting in the structure shown in Figure S1(e), and observing that the defect does not result in significant structural deformations.

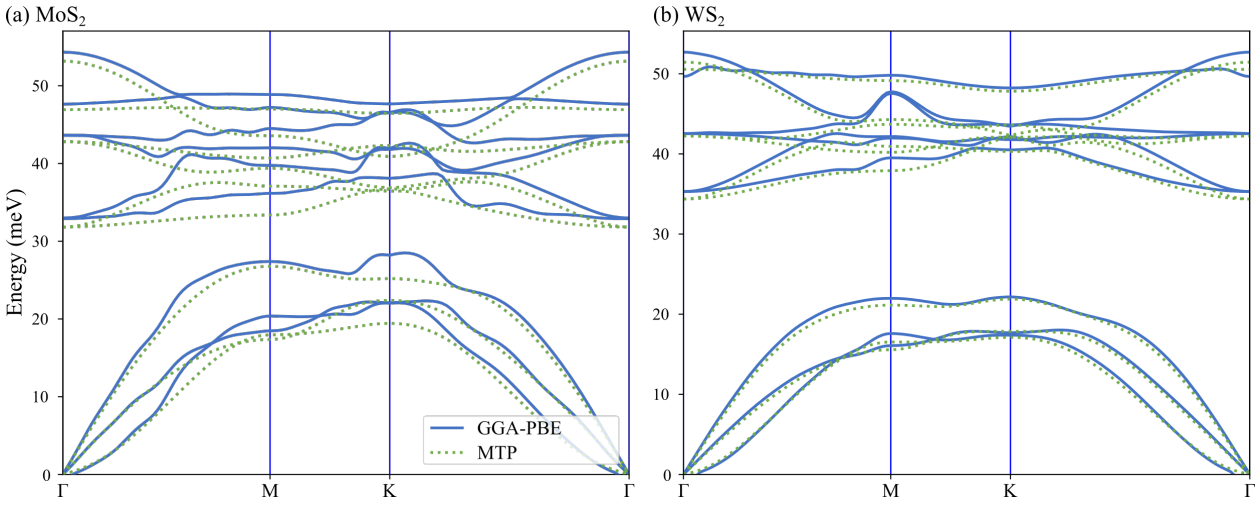

Figure S2: Phonon dispersion diagram for the fully relaxed 1L- (a) MoS_2, (b) WS_2 unit cells.

Table S2: Comparison of the fully relaxed lattice parameters ($a_1 = a_2$ in units of Å) for MoS_2 and WS_2 unit cells.

System	DFT	MTP
MoS_2	3.248765	3.319738
WS_2	3.256730	3.254932

Calculation of thermal conductivity

We setup the following MD sequence for calculating the thermal conductivity, κ, with the NEMD method: *i*) 100 ps under the canonical ensemble (NVT) to slowly increase the temperature of the system to 300K, *ii*) 100 ps of volume relaxation at 300K under the isothermal–isobaric ensemble (NPT), *iii*) 100 ps of aditional NVT at 300K for thermal equilibration, and *iv*) 1 ns of non-equilibrium momentum exchange under the microcanonical ensemble (NVE). The latter is used for obtaining the average heat current of each case and produce a temperature profile during the last 500 ps of the simulation.

We now show an example of the κ calculation for a 1L-MoS_2 system of length $l = 132$ nm using the NEMD method and comparing the trained MTP with the SW potential in.[5] Figure S3(a) shows the heat current from source to drain terminals $\langle dQ/dt \rangle$ during 1 ns of non-equilibrium momentum exchange, where we obtain average values of 0.968 and 0.878 eV/ps for SW and MTP, respectively. As observed in Figure S3(b), we obtain the temperature

profile of the sample during the last 500 ps of the MD run and calculate the differential of temperature over distance $\langle dT/dz \rangle$ in the middle of the system, where we can approximate a linear fitting with slope of -0.238 and -0.376 K/nm for SW and MTP, respectively. Then, we estimate a cross-sectional area $S = 15.26$ nm^2, assuming a monolayer thickness of 0.6033 nm and a width of 25.3 nm. Lastly, we compute $\kappa = -(1/S)\langle dQ/dt \rangle / \langle dT/dz \rangle$, which results in 42.56 and 24.48 WK^{-1}m^{-1} for SW and MTP, respectively. These results are then used to extrapolate the infinite thermal conductivity, κ_∞, as discussed in the main text.

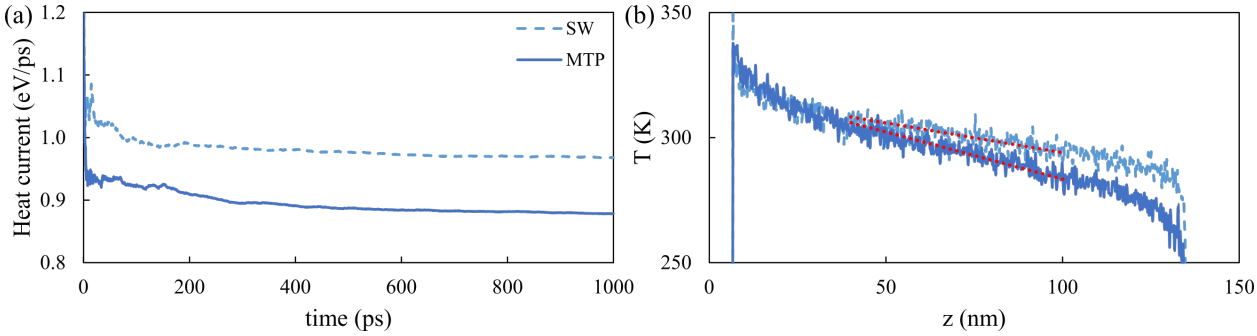

Figure S3: (a) Heat current and (b) temperature profile of a 1L-MoS_2 sample of length $l =$ 132 nm, comparing the trained MTP with SW calculations.

On the other hand, the NEGF calculates the thermal conductance, σ, by obtaining the phonon transmission spectrum from the phonon Green's function $\boldsymbol{G}(\omega)$, which is mathematically similar to the calculation of electron currents with the electron Green's function $\boldsymbol{G}(E)$, but using the diagonal matrix with the element masses $\boldsymbol{M}$ (instead of the identity matrix $\boldsymbol{I}$) and the dynamical matrix of the central region $\boldsymbol{K}_C$ (instead of the Hamiltonian $\boldsymbol{H}_C$), which is connected to two semi-infinite, defect-free regions, one to the left and one to the right, with self-energy matrices $\boldsymbol{\Sigma}_{L,R}(\omega)$.[6]

After calculating κ for the finite length systems, we obtain the thermal conductivity of infinite systems, κ_∞, by extrapolating κ with the expression: $1/\kappa = (1 + \Lambda/l)/\kappa_\infty$,[7–9] where l is the length of the sample and Λ is the effective phonon mean free path, assumed to be 100 nm in all cases. Table S3 summarizes our results for 1L-MoS_2 and 1L-WS_2 systems, and compares with previous measurements and calculations of κ.

Table S3: Experimental and theoretical thermal conductivity of 1L-MoS_2 and 1L-WS_2

TMD	Method	κ ($WK^{-1}m^{-1}$)
MoS_2	Temperature-dependent Raman	34.5±4 [10]
	Time-resolved spectroscopy	74±21 [11]
	Opto-thermal Raman	84±17 [12]
	NEMD	1.35 [13]
	NEMD	18.06 [14]
	NEGF	23.2 [15]
	Slack	33.6 [16]
	NEMD	38.1 [17]
	NEMD - MTP (this work)	43.2
	NEGF - SW (this work)	66.1
	NEGF - MTP (this work)	63.4
	NEMD - SW (this work)	75.1
	BTE	83 [18]
	BTE	103 [19]
	BTE	131 [20]
WS_2	Temperature-dependent Raman	32 [21]
	Slack	31.8 [16]
	NEGF - MTP (this work)	33.7
	NEMD - MTP (this work)	51.4
	BTE	142 [19]

References

(1) Shapeev, A. V. Moment tensor potentials: A class of systematically improvable interatomic potentials. *Multiscale Modeling and Simulation* **2016**, *14*, 1153–1173.

(2) QuantumATK version S-2021.06-SP1, Synopsys QuantumATK (https://www.synopsys.com/silicon/quantumatk.html).

(3) Smidstrup, S. et al. QuantumATK: An integrated platform of electronic and atomic-scale modelling tools. *Journal of Physics Condensed Matter* **2020**, *32*.

(4) Perdew, J. P.; Burke, K.; Ernzerhof, M. Generalized Gradient Approximation Made Simple. *Phys. Rev. Lett.* **1996**, *77*, 3865–3868.

(5) Jiang, J.-W.; Park, H. S.; Rabczuk, T. Molecular dynamics simulations of single-layer molybdenum disulphide (MoS2): Stillinger-Weber parametrization, mechanical properties, and thermal conductivity. *Journal of Applied Physics* **2013**, *114*, 064307.

(6) Markussen, T.; Jauho, A.-P.; Brandbyge, M. Electron and phonon transport in silicon nanowires: Atomistic approach to thermoelectric properties. *Phys. Rev. B* **2009**, *79*, 035415.

(7) Schelling, P. K.; Phillpot, S. R.; Keblinski, P. Comparison of atomic-level simulation methods for computing thermal conductivity. *Physical Review B* **2002**, *65*, 144306.

(8) Zhang, X.; Xie, H.; Hu, M.; Bao, H.; Yue, S.; Qin, G.; Su, G. Thermal conductivity of silicene calculated using an optimized Stillinger-Weber potential. *Physical Review B* **2014**, *89*, 054310.

(9) Mortazavi, B.; Podryabinkin, E. V.; Novikov, I. S.; Roche, S.; Rabczuk, T.; Zhuang, X.; Shapeev, A. V. Efficient machine-learning based interatomic potentialsfor exploring thermal conductivity in two-dimensional materials. *JPhys Materials* **2020**, *3*.

(10) Yan, R.; Simpson, J. R.; Bertolazzi, S.; Brivio, J.; Watson, M.; Wu, X.; Kis, A.; Luo, T.; Hight Walker, A. R.; Xing, H. G. Thermal conductivity of monolayer molybdenum disulfide obtained from temperature-dependent Raman spectroscopy. *ACS nano* **2014**, *8*, 986–993.

(11) Kim, T.; Ding, D.; Yim, J.-H.; Jho, Y.-D.; Minnich, A. J. Elastic and thermal properties of free-standing molybdenum disulfide membranes measured using ultrafast transient grating spectroscopy. *APL Materials* **2017**, *5*, 086105.

(12) Zhang, X.; Sun, D.; Li, Y.; Lee, G.-H.; Cui, X.; Chenet, D.; You, Y.; Heinz, T. F.; Hone, J. C. Measurement of lateral and interfacial thermal conductivity of single-and bilayer MoS2 and MoSe2 using refined optothermal Raman technique. *ACS applied materials & interfaces* **2015**, *7*, 25923–25929.

(13) Liu, X.; Zhang, G.; Pei, Q.-X.; Zhang, Y.-W. Phonon thermal conductivity of monolayer MoS2 sheet and nanoribbons. *Applied Physics Letters* **2013**, *103*, 133113.

(14) Varshney, V.; Patnaik, S. S.; Muratore, C.; Roy, A. K.; Voevodin, A. A.; Farmer, B. L. MD simulations of molybdenum disulphide (MoS2): Force-field parameterization and thermal transport behavior. *Computational Materials Science* **2010**, *48*, 101–108.

(15) Cai, Y.; Lan, J.; Zhang, G.; Zhang, Y.-W. Lattice vibrational modes and phonon thermal conductivity of monolayer MoS2. *Physical Review B* **2014**, *89*, 035438.

(16) Peng, B.; Zhang, H.; Shao, H.; Xu, Y.; Zhang, X.; Zhu, H. Thermal conductivity of monolayer MoS 2, MoSe 2, and WS 2: interplay of mass effect, interatomic bonding and anharmonicity. *RSC advances* **2016**, *6*, 5767–5773.

(17) Krishnamoorthy, A.; Rajak, P.; Norouzzadeh, P.; Singh, D. J.; Kalia, R. K.; Nakano, A.; Vashishta, P. Thermal conductivity of MoS2 monolayers from molecular dynamics simulations. *AIP Advances* **2019**, *9*, 035042.

(18) Li, W.; Carrete, J.; Mingo, N. Thermal conductivity and phonon linewidths of monolayer MoS2 from first principles. *Applied Physics Letters* **2013**, *103*, 253103.

(19) Gu, X.; Yang, R. Phonon transport in single-layer transition metal dichalcogenides: A first-principles study. *Applied Physics Letters* **2014**, *105*, 131903.

(20) Gandi, A. N.; Schwingenschlögl, U. Thermal conductivity of bulk and monolayer MoS2. *EPL (Europhysics Letters)* **2016**, *113*, 36002.

(21) Peimyoo, N.; Shang, J.; Yang, W.; Wang, Y.; Cong, C.; Yu, T. Thermal conductivity determination of suspended mono-and bilayer WS2 by Raman spectroscopy. *Nano Research* **2015**, *8*, 1210–1221.